Materials and Design 153 (2018) 129–138

Contents lists available at ScienceDirect

Materials and Design

journal homepage: www.elsevier.com/locate/matdes

Selective laser remelting of an additively manufactured Cu-Al-Ni-Mn shape-memory alloy

Tobias Gustmann *, Holger Schwab, Uta Kühn, Simon Pauly *

IFW Dresden, Institute for Complex Materials, 01069 Dresden, Germany

HIGHLIGHTS

- Selective laser remelting enhances the relative density of Cu-11.85Al-3.2Ni-3Mn shape-memory parts.
- The grain size can be modified during remelting.
- The transformation temperatures can be adjusted in a broad range via remelting.
- Selective laser remelting is a promising approach for optimizing the properties of shape-memory alloys.

GRAPHICAL ABSTRACT

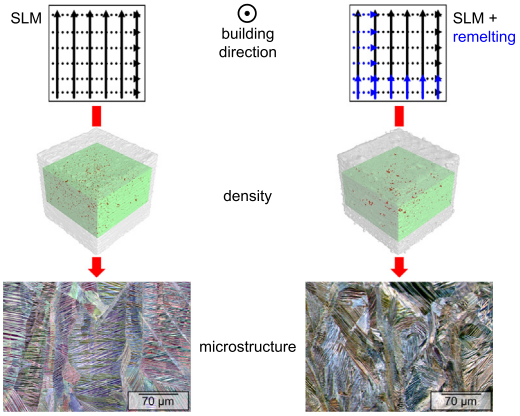

ARTICLE INFO

Article history:
Received 4 February 2018
Received in revised form 23 April 2018
Accepted 4 May 2018
Available online 5 May 2018

Keywords:
Additive manufacturing
Selective laser melting
Laser remelting
Shape-memory alloy
Microstructure
Mechanical properties

ABSTRACT

Selective laser melting (SLM) was used to manufacture fully martensitic (β'_1) samples of the shape-memory alloy 81.95Cu-11.85Al-3.2Ni-3Mn (wt%). Crack-free specimens with a high relative density of about 98.9 ± 0.1% were produced. Immediate remelting of already processed layers during SLM enhances the relative density (99.5 ± 0.3%). Primarily by varying the scanning speed in the remelting step, the thickness of the remelted zone can be adjusted. Moreover, remelting alters the microstructure as well as the transformation temperatures, which tend to rise with the volumetric energy input. In this way, the shape-memory properties can be modified without compromising the relative density and the considerable plasticity of the samples. Thus, the remelting procedure proves to be an interesting tool for 81.95Cu-11.85Al-3.2Ni-3Mn and related alloys in order to optimize and tailor their performance already during SLM processing and without applying additional post-processing steps.

1. Introduction

Selective laser melting (SLM) is a laser-based additive manufacturing technique in which a bulk part is created layer-by-layer through melting defined areas of a powder bed [1–4]. In general, SLM is used for the fabrication of metallic components with a high degree of geometrical freedom and often yields materials properties comparable or

* Corresponding authors.
E-mail addresses: t.gustmann@ifw-dresden.de, (T. Gustmann), s.pauly@ifw-dresden.de (S. Pauly).

https://doi.org/10.1016/j.matdes.2018.05.010
0264-1275/

even superior to their conventionally processed counterparts [3,5–8]. Another considerable benefit is that the processing of a thin powder layer (generally between 20 and 100 μm) on massive substrate plates in combination with small laser spot diameters results in high intrinsic cooling rates [2]. These unique processing conditions have a strong impact on the microstructure (grain refinement) and, in turn, this can enhance the performance of additively manufactured materials [6].

One key aspect in SLM is the resulting porosity, which can be relatively high compared to conventionally processed material. Because of its versatility a large number of process parameters can be varied during selective melting most of which influence the final density and the properties of a part [3,9]. Despite the difficulties in optimizing the SLM processing parameters for obtaining high-quality parts, the general applicability and potential of SLM has been already demonstrated for a variety of alloys [2–4,6,7,10,11]. Among these materials, shape-memory alloys (SMAs) are one group of materials that have drawn attention due to new and innovative actuator designs that are now feasible to be produced in a cost effective way via SLM [12–14].

The most widely used and studied SMA for applications, equiatomic NiTi (Nitinol), has been already processed via SLM by numerous groups and the capability of this approach in terms of manufacturing medical devices has been shown [13–20]. However, industrial use of Nitinol is limited due to transformation temperatures below 100 °C [21,22]. Extensive research has been carried out to increase the transformation temperatures by developing new alloy compositions that can be applied at temperatures above 100 °C, the so-called high-temperature shape-memory alloys (HTSMAs) [23]. But especially promising HTSMAs based on NiTi, viz. Ti-Ni-Pd, Ti-Ni-Pt or Ni-Ti-Hf, are relatively expensive and difficult to manufacture [22,24,25]. For example, the HTSMA Ni-Ti-Hf was recently produced by SLM [21]. These samples suffered from porosity, cracking and a significant oxygen uptake, which are inherent challenges when NiTi-based SMAs are being processed by SLM.

With regard to HTSMAs, there is a major interest in materials derived from Cu-based SMAs (e.g. Cu-Al-Ni-Mn [26]) due to their relatively low manufacturing costs, good processability as well as promising shape-memory properties [24,26–28]. The improved thermodynamic stability and a broad regime of transformations temperatures above 100 °C is characteristic for the family of Cu-Al-Ni-based alloys and has drawn interest in terms of applications [28]. Yet, the applicability of these alloys is limited by their brittleness in the coarse-grained polycrystalline state, which is caused by a strong elastic anisotropy and the precipitation of certain intermetallic phases [29,30]. Thus, intensive research was conducted in the processing of Cu-based SMAs with small grain sizes to overcome the poor deformability resulting from intergranular cracking [26,27,31–33]. Besides refining the microstructure through the addition of grain refiners such as Ti [26,28,33] or Zr [26], another approach constitutes in rapid solidification techniques like melt spinning [33], spray-forming [27] and SLM [34].

As shown previously [34,35], a Cu-Al-Ni-Mn shape-memory alloy can be successfully processed by SLM. An optimized parameter setup has been developed to obtain crack-free and fully martensitic (β'_1) specimens with a high relative density of up to 99%, low oxygen content, small grain sizes between 10 and 80 μm and transformation temperatures above 100 °C [1,36]. Although the relative density has been found to be very high in Cu-Al-Ni-Mn parts for a range of energy inputs [1], optimization to 100% relative density has not been feasible. The mechanical properties (i.e. deformability, yield strength) strongly depend on the remaining porosity, especially when it comes to fatigue [5]. One method to reduce or eliminate remaining defects (pores, cracks) in SLM parts without drastically changing the chemical composition or the phase formation of the material [37,38], is to employ a second laser process such as re-scanning or remelting of previously solidified layers [5,6,39–41]. This step can be easily implemented in the SLM process and is also called selective laser remelting (SLRM) [1].

The transformation temperatures of Cu-based SMAs strongly depend on the (i) chemical composition [26,31,42], (ii) the phases present [28] and (iii) the grain size [36,43,44]. For example, it has been reported that SLM processing, in contrast to manufacturing via spray forming, reduces the transformation temperatures due to a smaller grain size [36]. Furthermore, the transformation temperatures of Cu-based SMAs can be adjusted to higher values by changing the process parameters, viz. increasing the energy input during the manufacturing of SLM bulk samples [43]. Similar investigations have been reported for equiatomic NiTi alloys [12,15–17,20]. Interestingly, the possibility of an additional remelting step to further optimize and adjust the properties of SMAs has not been investigated so far. This makes employing an additional remelting step in the SLM process a very interesting approach, because the main parameters for remelting like laser power, scanning speed and track overlap result in additional energy dissipated in previously solidified layers and should affect the grain size and with it the transformation temperatures.

In this study, the SLM process has been combined with an additional remelting step to process the shape-memory alloy 81.95Cu-11.85Al-3.2Ni-3Mn (wt%). The remelting step is implemented in order to further increase the relative density. The main focus of this work, yet, is to study the effect of the additional remelting step on the microstructure and the transformation characteristics. Therefore, we correlate the influence of the additional energy input with the microstructural details (e.g. phase formation, grain size), the corresponding transformation temperatures and the mechanical properties.

2. Experimental details

2.1. Materials and processing

The Cu-based shape-memory alloy 81.95Cu-11.85Al-3.2Ni-3Mn (wt%) was processed by selective laser melting in a SLM 250^{HL} (SLM Solutions Group AG) equipped with a 400 W Nd:YAG-based fibre laser. Based on our previous work [1], an optimized parameter setup with a laser power (P_L) of 330 W (wavelength $\lambda = 1.064$ μm, laser spot diameter = 80 μm), a scanning speed (v_s) of 740 mm/s and a track overlap of 30% (hatching distance (h_c) = 0.13 mm) was selected by using a stripe-hatching strategy (rotation per layer: 90°) and a layer thickness of 90 μm for the fabrication of SLM bulk samples with various geometries (cubes, rods and beams). The powder used had a particle size between 30 and 90 μm ($d_{50} = 48$ μm) and is suitable for the SLM process as described in [1].

During manufacturing of particular SLM samples, every layer was additionally illuminated by the laser [1] in order to remelt the material with various scanning speeds and track overlaps. First, the processing parameters for the additional remelting procedure were optimized in single-track experiments on a 81.95Cu-11.85Al-3.2Ni-3Mn baseplate. The laser power was varied between 300 and 340 W (laser spot diameter = 130 μm) and the scanning speed was altered between 500 and 2500 mm/s. The width and morphology of the individual tracks was measured using a digital microscope (Keyence VHX-2000). Subsequently, bulk material with a surface area of 4×4 mm^2 was remelted at a constant laser power ($P_L = 330$ W) with scanning speeds and track overlaps between 500 and 1500 mm/s as well as 30 and 90%, respectively. The remelting depth of the remelted surfaces was measured along the cross-sections using an optical microscope (Nikon Epiphot 300). In the next step, the same parameter combinations were applied to SLM bulk samples in order to remelt previously processed layers. These samples will be abbreviated as SLRM.

2.2. Sample characterization

The chemical composition of the powder and the bulk material was analyzed using ICP-OES (Inductively-Coupled Plasma-Optical Emission Spectroscopy, IRIS Intrepid II XUV, Thermo Fischer Scientific).

The density of all specimens was measured via the Archimedean method using a Sartorius MC210P balance. Relative densities were

calculated by relating them to the density of a defect-free induction-cast sample [1]. Selected SLM and SLRM specimens were investigated using X-ray computed tomography (μ-CT, General Electric Phoenix nanotom m). The resolution of the μ-CT was adjusted to 8 μm. 1600 projections were recorded for each reconstruction and the volume analysis was conducted using the software VG-Studio (Volume Graphics). Between 1000 and 3000 individual pores were analyzed (minimal size: 5 voxel) in order to obtain the present pore size distribution.

Microstructural investigations were carried out using an optical microscope (Nikon Epiphot 300). The obtained micrographs in building direction were evaluated with the software ImageAccess after etching ($HNO_3 + H_2O$) by linear intercepts to obtain the grain size as well as the length and width of the grains according to the ASTM E112 and DIN EN ISO 643 standards. Further investigations from the centre of the specimens were performed by scanning electron microscopy (SEM) using a Gemini Leo 1530. In addition, EBSD analysis was conducted using a Bruker e⁻Flash 1000 detector including a forescattered/backscattered electron imaging system (ARGUS™) for colour-coded visualization of the grain orientation. The phase and grain size determination were realized with the Bruker software Esprit 2.0 by applying a misorientation criterion of 15° and a minimum of 2 pixels for the detection of the smallest grains.

The transformation temperatures were investigated by differential scanning calorimetry (DSC) in a Perkin Elmer DSC-7 and a Netzsch DSC-404C at a heating and cooling rate of 10 K/min. All samples were cycled between 40 and 180 °C, whereas selected samples were heated up to a maximum temperature of 850 °C in order to investigate the DO_3-B2 ordering temperature and the corresponding enthalpy.

Mechanical characterization was conducted in an INSTRON 5869 under a constant strain rate of 5×10^{-4} s^{-1}. The strain during all mechanical tests was recorded by a laser extensometer (Fiedler Optoelektronik). The tensile samples, SLM beams with dimensions of $8 \times 8 \times 40$ mm^3 were machined as flat tensile samples [43] by electrical discharge machining. Cylindrical compression test samples having a height of 6 mm and a diameter of 3 mm were also machined and ground coplanar.

3. Results and discussion

The following discussion is divided into four parts. First, we will address the systematic development of the process parameters for the additional remelting step. Afterwards, we elaborate on how different remelting parameters affect the relative density of the manufactured samples. The third section focuses on the interrelation between the energy input during remelting and the microstructure whereas the martensitic transformation as well as the mechanical properties are discussed in the end.

3.1. Optimization of the remelting parameters

In analogy to single-track experiments, which are often used as a starting point for optimizing the SLM parameters [3,6,11,12], we first remelted a 81.95Cu-11.85Al-3.2Ni-3Mn baseplate along individual lines [34]. The remelting width and the morphology of the tracks are strongly affected by the energy input [1,36]. The volumetric energy input during SLM processing, E_V, can be estimated as [1,6,15,36]:

$$E_V = \frac{P_L}{v_s \cdot h_c \cdot l_z} \quad (1)$$

with P_L: laser power, v_s: scanning speed, h_c: hatching distance (defining the track overlap) and l_z: powder layer thickness. The process parameters used for the SLM reference samples are $P_L = 330$ W, $v_s = 740$ mm/s, $h_c = 0.13$ mm (30% track overlap) and $l_z = 90$ μm [1]. In the case the bulk material is remelted as a one-dimensional line, Eq. (1) can be adapted to calculate the energy deposited in a single track (E_T):

$$E_T = \frac{P_L}{v_s} \quad (2)$$

The remelting track width as a function of the energy line input, E_T, is shown in Fig. 1a. In addition, Fig. 1b–d depict the remelting tracks of selected parameter combinations. In the investigated energy regime there is an almost linear relationship between the track width and the deposited energy. At relatively high energy line densities (above E_T = 0.5 J/mm) the remelting tracks are uniform and rather broad (Table 1, Fig. 1b). If the energy input is lowered (E_T = 0.2–0.5 J/mm) the tracks become narrower. However, a continuous morphology can be still observed (Fig. 1c). When E_T falls below 0.2 J/mm the tracks begin to become discontinuous (fragmented droplets, Fig. 1d). The energy dissipated in the track under these conditions is too low to form a continuous melt pool. This is comparable to the balling-effect observed

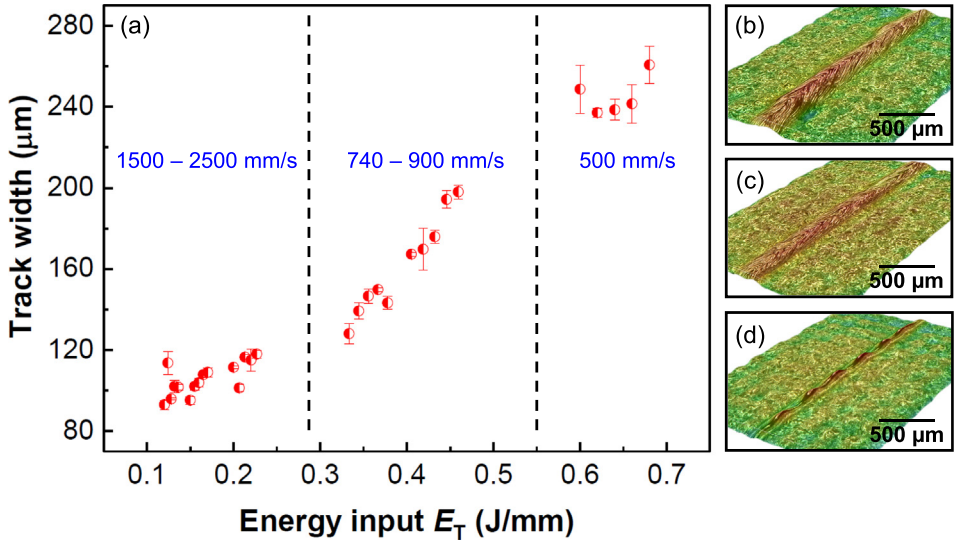

Fig. 1. Influence of the energy input, E_T, on the width of the remelting tracks (a). The experiments were carried out with different laser powers (P_L = 300–340 W) and scanning speeds (v_s = 500–2500 mm/s). The track morphologies can be classified as (b) wide and smooth (P_L = 330 W, v_s = 500 mm/s, E_T = 0.66 J/mm), (c) narrow and continuous (P_L = 330 W, v_s = 740 mm/s, E_T = 0.45 J/mm) and (d) narrow and discontinuous (P_L = 330 W, v_s = 1500 mm/s, E_T = 0.22 J/mm). Please note that the track height is digitally enhanced in order to more accurately determine the track width.

Table 1
Overview of selected process parameters for remelting track experiments and remelting a surface area of 4 × 4 mm² bulk material with a laser power of 330 W. The influence of the process parameters on the remelting coefficient (R_C) can be seen in Fig. 2.

Scanning speed (mm/s)	Energy input E_T (J/mm)	Track width (μm)	Hatching distance h_r (mm)	Track overlap (%)	R_C
500	0.66	241 ± 10	0.17	30	2.3 ± 0.5
			0.12	50	1.8 ± 0.3
			0.06	75	2.3 ± 0.5
			0.03	90	2.6 ± 0.3
740	0.45	194 ± 4	0.14	30	0.9 ± 0.2
			0.10	50	1.2 ± 0.2
			0.05	75	1.5 ± 0.2
			0.02	90	1.4 ± 0.1
900	0.37	150 ± 1	0.11	30	0.7 ± 0.2
			0.08	50	0.9 ± 0.2
			0.04	75	1.3 ± 0.2
			0.02	90	1.4 ± 0.1
1500	0.22	115 ± 6	0.09	30	0.7 ± 0.1
			0.06	50	0.6 ± 0.1
			0.03	75	0.6 ± 0.1
			0.01	90	0.5 ± 0.1

during SLM processing of single tracks under certain conditions [1,3,6,12]. Only those process parameters, which resulted in continuous tracks (P_L = 330 W, v_s = 500–1500 mm/s) were used for remelting the 81.95Cu-11.85Al-3.2Ni-3Mn bulk material. More specifically, we selected parameters corresponding to intermediate energy line densities of 0.22 J/mm < E_T < 0.66 J/mm and track overlaps of 30–90%.

All remelted volumes revealed a homogenous shape underneath the surface with a rather uniform remelting depth (cf. Table 1). In addition, no pores or keyholes were found. The depth of the remelted zone depends on the processing parameters (Fig. 2) and in order to quantify it we introduce the remelting coefficient, R_C, which is defined as the depth of the remelted layer (t_r) normalized by the layer thickness (l_z):

$$R_C = \frac{t_r}{l_z} \tag{3}$$

Fig. 3 summarizes the variation of the remelting coefficient with the scanning speed and the hatching distance (h_r, see Section 3.2). There is a clear correlation between the scanning speed and the remelting coefficient irrespective of the track overlap. As expected, the higher the scanning speed, the smaller the remelted layer because less heat is deposited in the system. Interestingly, the track overlap has no distinct influence on the thickness of the remelted layer. This becomes especially obvious from the inset to Fig. 3; R_C strongly scatters when plotted against the hatching distance. It seems that the system does not accumulate substantial amounts of heat after each track is completed owing to the scanning strategy, the relative high scanning speeds and large sample size. Every melt track has already solidified when the neighbouring track is produced and, thus, the volume, which is melted on laser illumination, remains virtually unchanged (cf. R_C in Table 1).

Generally, R_C ranges between 0.5 and 2.6, which means that significantly different volumes can be remelted and that the solidification and with it the microstructure should be measurably affected. We will address this in Section 3.3.

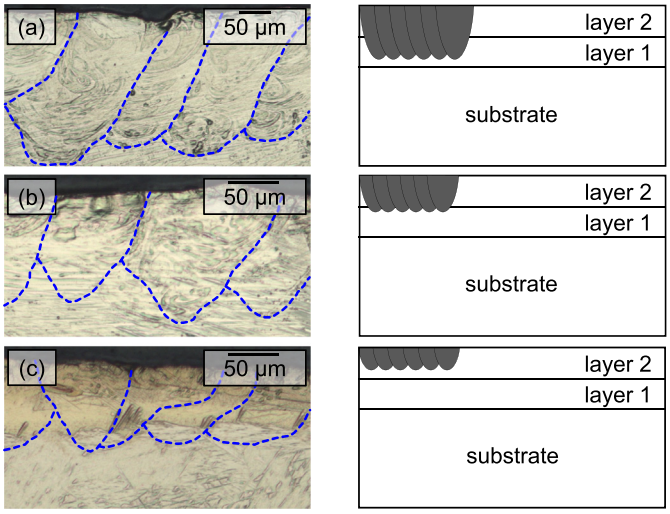

Fig. 2. Cross-sections of Cu-Al-Ni-Mn-baseplates showing the remelted layers and the individual weld beads (dashed lines) for three different parameter setups (P_L = 330 W): (a) v_s = 500 mm/s, 50% track overlap, (b) v_s = 740 mm/s, 50% track overlap and (c) v_s = 1500 mm/s, 30% track overlap. The remelting depth is 163 ± 50 μm, 105 ± 30 μm and 65 ± 10 μm, respectively. In case of SLRM, the corresponding remelting of previously solidified layers by SLM is depicted schematically on the right-hand side (R_C: 1.8, 1.2 and 0.7, respectively).

3.2. Density and pore size distribution

The parameter combinations of the aforementioned remelting experiments were transferred to the SLM fabrication of 81.95Cu-11.85Al-3.2Ni-3Mn bulk samples. In an attempt to correlate the process parameters with the relative density we will refer to the energy input during remelting, $E_{V,r}$, which combines scanning speed and hatching distance (cf. eq. 1). Because solid material is remelted, we have to consider a slightly different hatching distance (h_r, see Table 1) than for the SLM process (h_c) itself. Therefore, Eq. 1 has to be adapted for the remelting procedure as:

$$E_{V,r} = \frac{P_L}{v_s \cdot h_r \cdot l_z} \tag{4}$$

In the investigated parameter window, the relative density does not show any clear correlation with the remelting depth, the energy input ($E_{V,r}$) or either of the varied processing parameters (cf. Table 2). It is noteworthy that when a sample is remelted with v_s = 740 mm/s and 30% track overlap (SLRM (2), Table 2), which corresponds to an energy input of 35.4 J/mm³, the relative density is highest (ρ_{rel} = 99.5 ± 0.3%). Remelting, consequently, allows increasing the relative density of the alloy compared to the SLM sample (ρ_{rel} = 98.9 ± 0.1%) but finding the optimum remelting parameters in terms of relative density seems a matter of trial and error.

It has been suggested that the additional remelting step enhances the relative density mainly due to the elimination of pores smaller 50 μm [1] and improving the surface quality [3,39]. In order to investigate the first aspect for the present alloy, the pore sizes and the pore distribution in selected specimens were determined in a μ-CT. The according μ-CT scans and the extracted pore size distributions are displayed in Fig. 4. The vast majority of the pores in the SLM samples has equivalent diameters of

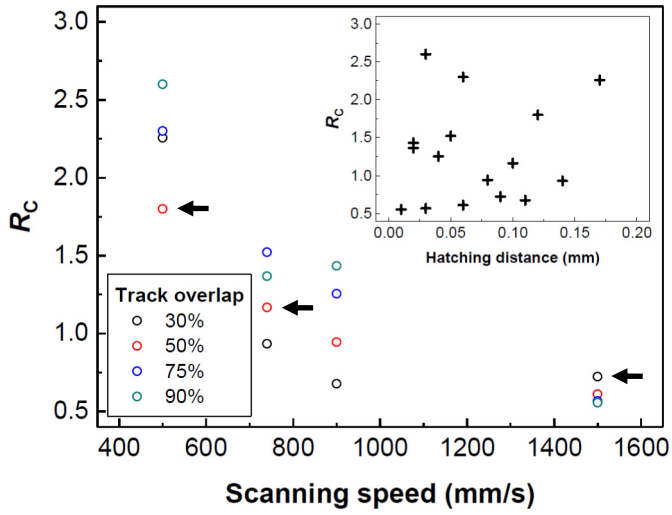

Fig. 3. Influence of the process parameters (P_L = 330 W) during remelting of a 81.95Cu-11.85Al-3.2Ni-3Mn baseplate on the remelting coefficient, R_C. It is mostly determined by the scanning speed. The corresponding remelted cross-sections (arrows) are shown in Fig. 2. As the inset reveals, there is no clear correlation between the hatching distance (h_r) and the remelting coefficient.

0.1 mm (d_{90} = 0.09 mm). After remelting each layer with v_s = 740 mm/s and 30% track overlap, the population of smaller pores becomes less while larger pores appear (d_{90} = 0.11 mm). Because the relative density increases to 99.5 ± 0.3% this does not negatively affect the mechanical properties of the SLRM sample (see Section 3.5). When the remelting parameters are changed in way that $E_{V,\,r}$ and R_C are increased (v_s = 900 mm/s and 90% track overlap), the tail towards larger pore sizes in the distribution becomes even more evident (Fig. 4c). This trend reflects in a significantly larger d_{90}-value of 0.25 mm.

Hot isostatic pressing (HIP) is often used to reduce the porosity of cast solids [45] and it would be interesting to compare the effect of this post-treatment with the effect of the investigated remelting during selective laser melting. This, however, is not within the scope of the present work.

3.3. Microstructural analysis

The additional remelting procedure does not affect the phase formation of the Cu-Al-Ni-Mn alloy [1] and only β′$_1$-martensite (space group: P2$_1$/m, a = 0.443 nm, b = 0.530 nm, c = 1.278 nm and β = 95.88° [46,47]) forms in all SLM samples produced here. The decomposition into the low-temperature equilibrium phase γ_2 (Cu_9Al_4) is suppressed because of the high intrinsic cooling rates during processing [2,8,43]. Furthermore, the formation of oxides could be avoided due to the fact that the samples were prepared in argon atmosphere (oxygen uptake = 200 ppm).

The following discussion concentrates on the microstructures of the SLM, the SLRM (2) and the SLRM (6) sample. As mentioned above, the SLRM (2) specimen has the highest relative density (99.5 ± 0.3%) and the SLRM (6) sample was chosen because of its much higher energy input, which leads to a significantly higher remelting coefficient (R_C = 1.4 ± 0.1), as discussed in Section 3.2. In this way we want to investigate the influence of remelting, especially the effect of different energy inputs on the resulting microstructure. The microstructures, which were analyzed by means of EBSD along the building direction (BD), are shown in Fig. 5. The selected microstructures are characterized by grains elongated in the direction of the heat flow [19,36]. Some grains grow over multiple layers in an epitaxy-like manner [1] as described for other additively processed alloys [4,7,10,48]. Next to large grains also very fine grains can be found, as discussed in [1,36]. Moreover, the EBSD images of Fig. 5 illustrate that the martensite morphology is affected by remelting. After remelting the martensite laths tend to become initially smaller (Fig. 5b). Simultaneously, selected variants become longer and grow on the expense of others. Hence, a change of the grain size is also reflecting in the corresponding variants [49] as it is observed here. This effect can be clearly seen if remelting is applied with a higher energy input as for the SLRM (6) sample. As shown in Fig. 5c, the microstructure tends to significantly coarsen under these conditions (average grain size: SLM = 45 ± 33 μm, SLRM (6) = 84 ± 41 μm). It should be stressed here that the highly non-uniform grain sizes together with the martensitic structure make it very difficult to reliably characterize the grain size in a quantitative fashion. Owing to the resulting scattering of the data we can only identify coarse trends in the following. We start by measuring the length of line intercepts with the grain boundaries along the building direction and perpendicular to it. Fig. 6 depicts the distribution of the intercept lengths perpendicular and parallel to the building direction for the SLM sample and the SLRM (6) specimen. It is apparent that the grains tend to be longer in the building direction and cover a wider range of grain sizes, which indicates the anisotropy of the present microstructures. This can be also captured by the grain aspect ratio (Table 3). The maximum observed intercept length in the building direction is near 200 μm for the SLM sample. The population of the intercept lengths becomes broader in both directions when each layer is remelted (Fig. 6a and b). In other words, the grains coarsen in the course of an additional illumination with a high energy input. Especially the intercept lengths in the building direction tend to increase (maximum value for SLRM (6): 300 μm) so that the epitaxy-like growth is enhanced by the remelting step. This is expected to affect the transformation properties of the alloy [16,27,33] and this aspect will be dealt with in the next section.

3.4. Transformation behaviour

Next to the grain size [44,49], the transformation temperatures of a given Cu-based shape-memory alloy are generally governed by factors like ordering [50], defect density [50,51] and phase composition [33,43].

We first investigate if there is a correlation between the remelting and the ordering of the alloy. A SLM and a SLRM (6) sample were heated to 850 °C in order to analyse the enthalpy of ordering transition from DO_3 to B2 [50] that was measured around 500 °C. It is known that ageing

Table 2
Overview of a SLM sample and SLRM specimens processed with different scanning speeds and track overlaps (P_L = 330 W). Grain size values were recorded for two SLM geometries (cubes, rods) in building direction. The characteristic temperatures represent the peak-values of the reverse (A_{peak}) and forward (M_{peak}) martensitic transformation as well as the equilibrium temperature, T_0, from the second cycle.

Sample	Scanning speed (mm/s)	Track overlap (%)	Energy input $E_{V,\,r}$ (J/mm^3)	Relative density (%)	Average grain size (μm)	A_{peak} (°C)	M_{peak} (°C)	T_0 (°C)
SLM	740	30	38.1	98.9 ± 0.1	45 ± 33	102 ± 2	86 ± 1	98
SLRM (1)	500	30	43.1	98.9 ± 0.1	48 ± 29	91 ± 1	74 ± 1	92
SLRM (2)	740	30	35.4	99.5 ± 0.3	42 ± 24	96 ± 1	78 ± 1	92
SLRM (3)	900	30	37.0	99.2 ± 0.1	44 ± 25	95 ± 1	77 ± 1	91
SLRM (4)		50	50.9	98.6 ± 0.2	52 ± 28	92 ± 1	75 ± 1	90
SLRM (5)		75	101.9	97.5 ± 0.3	62 ± 32	103 ± 1	86 ± 1	102
SLRM (6)		90	203.7	98.1 ± 0.5	84 ± 41	118 ± 1	103 ± 1	117
SLRM (7)	1500	30	27.2	97.8 ± 0.1	46 ± 21	91 ± 1	74 ± 1	91

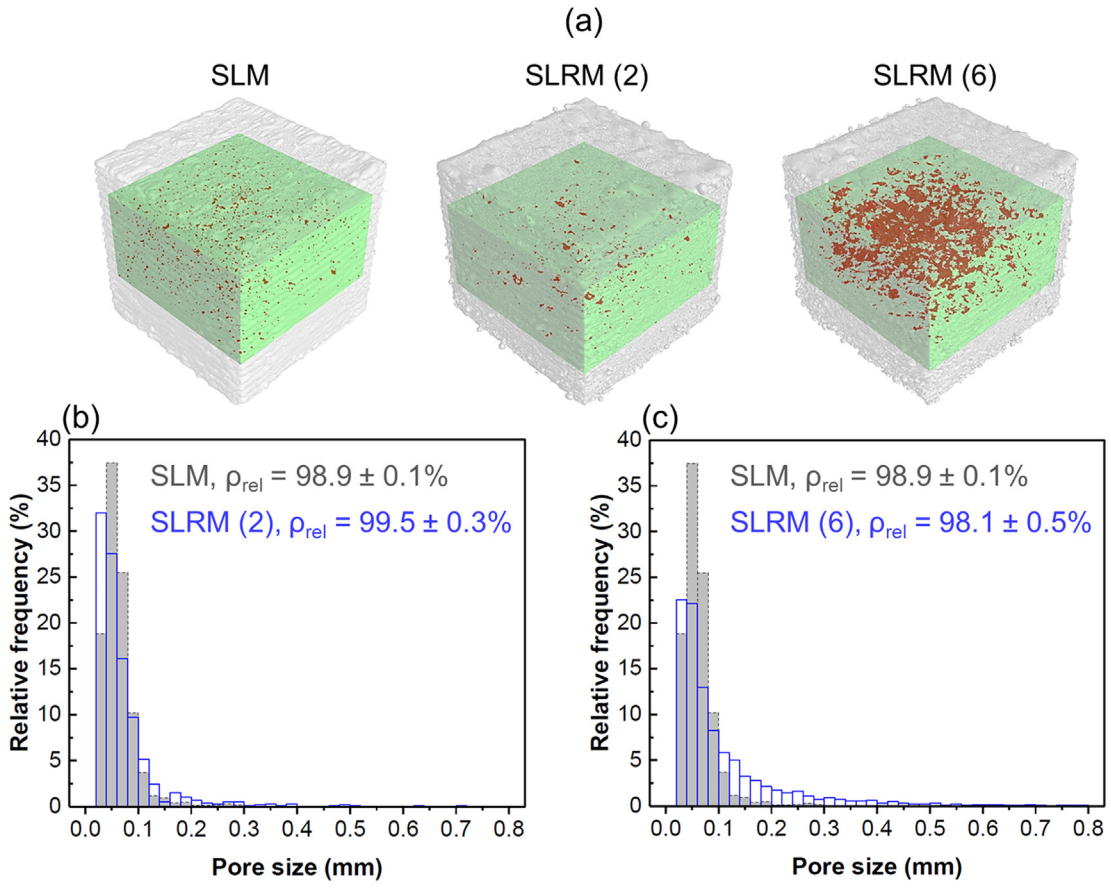

Fig. 4. Reconstruction of additively manufactured 81.95Cu-11.85Al-3.2Ni-3Mn cubes by μ-CT (a). The cubes correspond to SLM, SLRM (2) and SLRM (6) specimens (cf. Table 2). The analyzed volume (material: green, pores: red) was $7 \times 7 \times 5$ mm^3. The pore size distributions of the remelted samples in comparison to the SLM sample are shown in (b) and (c). Remelting at specific parameters (SLRM (2)) can effectively remove smaller pores. If the remelting energy is too high, the overall porosity increases and also larger pores will appear.

above the austenite-finish-temperature (A_f) can result in an increase of the transformation temperatures [52]. Specifically, an ordering process in the austenite leads to a shift of the transformation temperatures, which is usually accompanied by an increase in the enthalpy of the DO_3-B2 transition [50]. In the case of the investigated samples, no obvious differences were found for the enthalpy of the DO_3-B2 ordering process. The measured enthalpies were found to be 3.9 ± 0.2 J/g and 4.8 ± 0.1 J/g for the SLM (A_{peak}-temperature = 102 ± 2 °C) and SLRM (6) (A_{peak}-temperature = 118 ± 1 °C), respectively. Hence, this does not appear to be the dominant factor for the increase of the

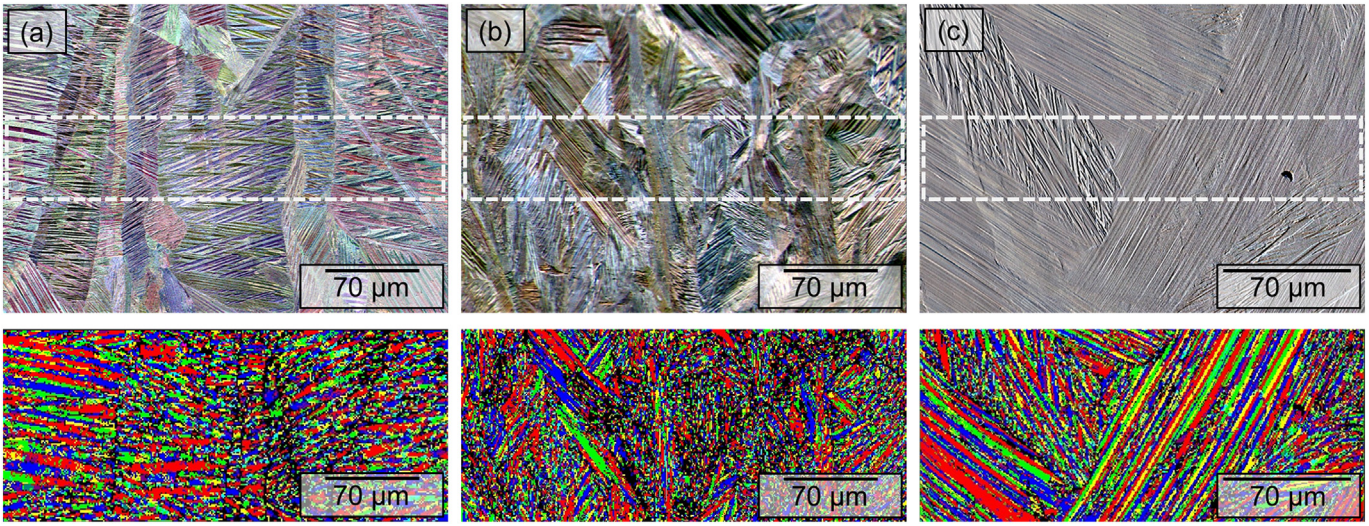

Fig. 5. EBSD-inspection of the cross-section of (a) the SLM and the SLRM specimens remelted with (b) lower (SLRM (2)) and (c) higher (SLRM (6)) energy input. The upper row shows an overview of the microstructure using the electron imaging system (ARGUS). The pictures in the second row represent an overview of the martensite variants determinations for the depicted areas. The equivalent size of variants are: SLM = 7.43 μm, SLRM (2) = 8.13 μm, SLRM (6) = 8.57 μm.

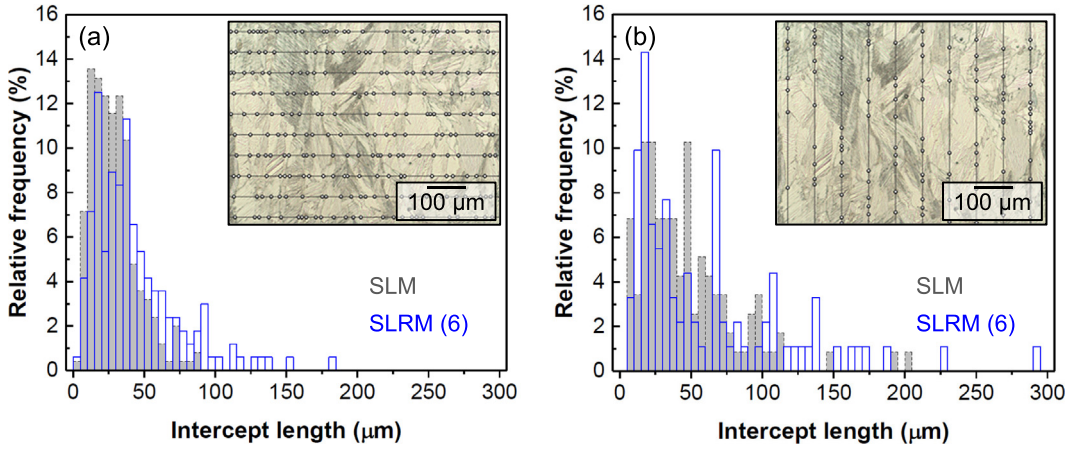

Fig. 6. Distribution of the intercept lengths of a SLM and a SLRM (6) sample. The histograms show the number of intercepts analyzed (a) perpendicular and (b) parallel to the building direction. The insets show a section of the SLM sample at its centre. The average intercept lengths were used for calculating the equivalent average grain size of the microstructure as summarized in Table 2.

transformation temperatures. Therefore, it shall be explored if there is a correlation between the grain size and the transformation behaviour.

In order to facilitate the following discussion, the intercept lengths, that are ideally suited for measuring non-equiaxed grains [53], are converted into the equivalent grain diameters using the grain-size data and relationships from the ASTM E112 standard. The ASTM micro-grain-size number, G, is used to estimate the average grain size. G can be calculated through the following equation [53]:

$$G = \left[-6.6457 \quad \log \bar{L}_3\right] - 3.298 \tag{5}$$

where $\bar{L}_3$ (mm) represents the average intercept length. The estimated values from the intercepts will be termed average grain size in the remainder. The average values are comparatively small for all investigated samples and range between 40 to 85 μm (Table 2) and are smaller than for other rapid solidification techniques, viz. suction casting [37] and spray forming [27]. Such small grains are generally favourable for enhancing the plasticity of Cu-based SMAs [30,35] and influence the transformation temperatures [44,49].

The peak-values of the reverse (A_{peak}) and forward (M_{peak}) transformation for the 81.95Cu-11.85Al-3.2Ni-3Mn specimens (SLM, SLRM) are listed in Table 2. It also contains the equilibrium transformation temperature, T_0, which is defined as the temperature when the Gibbs free energy of martensite and austenite is equal [43,54]:

$$T_0 = \frac{1}{2}\left(M_s + A_f\right) \tag{6}$$

with M_s: martensite-start-temperature and A_f: austenite-finish-temperature. The hysteresis for all samples between the austenitic (reverse) and the martensitic (forward) transformation is almost constant for the current samples (around 12 °C). Fig. 7 shows the variation of the A_{peak}-temperature as a function of the energy density used during SLM (reference bulk sample, red) and SLRM (blue). There is an apparent increase in A_{peak} with increasing energy input and depending on the remelting conditions, the transformation temperatures can be adjusted between 90 and 120 °C (cf. Table 2). This represents a drastic modification and proves the potential of the present approach for tailoring the transformation properties [15–17,20,43].

The transformation temperatures of Cu-based SMAs are very sensitive to the alloy composition [26,31,42] and remelting might locally result in a change of the chemical composition [38]. However, the oxygen uptake for the SLM and the SLRM samples is negligible (see Section 3.3) and the chemical composition of the SLM and the SLRM specimens are identical within the experimental error (SLM_{bulk}: 81.79Cu-11.84Al-3.21Ni-2.9Mn, SLRM $(2)_{bulk}$: 81.70Cu-11.84Al-3.22Ni-2.91Mn). Thus, an influence of alloy chemistry on the transformation temperatures can be excluded.

Fig. 7 contains the average grain sizes next to the transformation temperatures for the different specimens and a similar dependence on the energy input is found. One can deduce from the present data that an increasing energy input results in larger grains and thus in increased transformation temperatures. The transformation temperatures of Cu-based SMAs have been reported to obey a Hall-Petch-like relation [33]. The present results imply a similar behaviour. Selected SLRM samples with similar (v_s = 500–1500 mm/s, 30% track overlap) and more varying grain sizes (v_s = 900 mm/s, 30–90% track overlap) were correlated with the equilibrium temperature. As expected, the temperature shows no clear correlation when remelting parameters are applied that only slightly affect the microstructure. By continuously increasing the energy input and with it the grain size, an increase of T_0 can be achieved. Thus, our results show that remelting can be used to tailor the transformation temperatures directly during manufacturing by controlling the energy input. In the current case, an energy input, $E_{V,\,r}$, of about 204 J/mm^3 should be used for a maximum difference in the transformation temperatures which corresponds to the E_V-value used for a SLM bulk sample multiplied by a factor of 5.

Table 3
Microstructural and mechanical properties of the investigated SLM and SLRM specimens. SLRM samples with lower (P_L = 330 W, v_s = 740 mm/s, 30% track overlap, $E_{V,\,r}$ = 35.4 J/mm^3) and higher energy layer input (P_L = 330 W, v_s = 900 mm/s, 90% track overlap, $E_{V,\,r}$ = 203.7 J/mm^3) were chosen. The linear intercepts represent the average value for two geometries (cubes, rods) and were recorded parallel and perpendicular to the building direction.

	SLM	SLRM (2)	SLRM (5)	SLRM (6)
Perpendicular linear intercepts (μm)	28 ± 1	27 ± 2	41 ± 4	54 ± 10
Parallel linear intercepts (μm)	69 ± 16	53 ± 20	75 ± 11	114 ± 6
Grain aspect ratio (%)	243 ± 47	192 ± 60	181 ± 8	221 ± 52
Compressive fracture strength (MPa)	1511 ± 40	1512 ± 20	1200 ± 44	1440 ± 32
Compressive fracture strain (%)	14 ± 0.6	13 ± 1.0	11.6 ± 0.4	12.8 ± 0.4
Tensile fracture strength (MPa)	617 ± 48	492 ± 55	–	
Tensile fracture strain (%)	8.2 ± 0.9	9.3 ± 0.9		

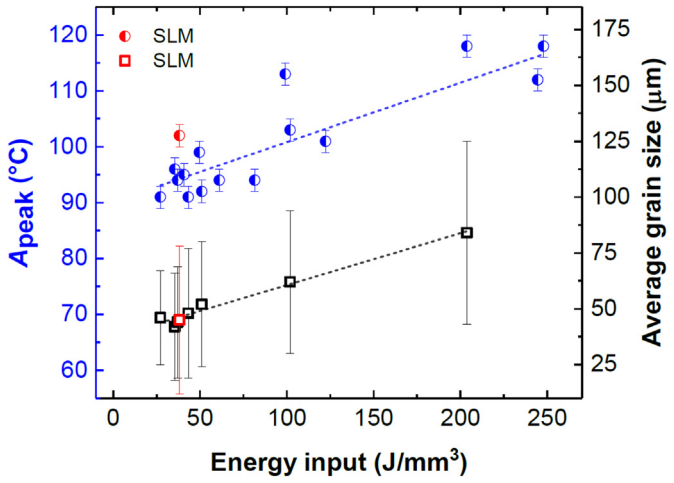

Fig. 7. Martensitic transformation of SLM and SLRM specimens. Correlation of the energy input (SLM: E_V and SLRM: $E_{V,\,r}$) on the A_{peak}-temperature and the average grain size of selected specimens. The values of the SLM sample are shown in red for comparison. The dashed lines are guides to the eye.

3.5. Mechanical properties

Final experiments were carried out to assess the mechanical behaviour of the SLM as well as selected SLRM (SLRM (2), (5) and (6)) specimens, since their different relative densities and grain size distributions could affect the deformation properties [5,30]. All samples were first subjected to uniaxial compression (Fig. 8a) and the corresponding values are specified in Table 3. The relative large fracture strain (11–15%) compared to other studies [31] can be attributed to the smaller grain sizes in the present study. The ultimate strength for all samples was found to be in the range of 1500 MPa. Due to the higher amount of pores and bigger pore sizes, the values of the SLRM (5) and (6) sample are found to be slightly below. In contrast to other studies [35], we have not observed a fracture strength much below 1200 MPa due to the overall high relative densities ($97.5 \pm 0.3\% < \rho_{rel} < 99.5 \pm 0.3\%$) of the tested samples. While the SLM sample yields the highest deformability ($14 \pm 0.6\%$), the SLRM samples are within the range of this value (SLRM (2) $= 13 \pm 1.0\%$, SLRM (5) $= 11.6 \pm 0.4\%$, SLRM (6) $= 12.8 \pm 0.4\%$). Hence, it becomes obvious that the differences in terms of the porosity on the fracture strain under the present conditions (compression) are not detrimental during deformation. This is even more interesting as the pores tend to be larger in the SLRM (6) specimens (Fig. 4c). A typical double yielding behaviour was observed showing a distinct elastic region, followed by a stress plateau (detwinning of martensite or reorientation) and a work hardening regime (plastic deformation of the martensitic microstructure) [31,35,43]. We found that the detwinning start stress (σ_s) of the SLRM in comparison to the SLM samples ($\sigma_{s,\,SLM} = 293 \pm 15$ MPa) is shifted towards lower values ($\sigma_{s,\,SLRM\,(2)} = 282 \pm 20$ MPa, $\sigma_{s,\,SLRM\,(5)} = 252 \pm 15$ MPa, $\sigma_{s,\,SLRM\,(6)} = 172 \pm 9$ MPa) which, in turn, seems to be consistent with the increasing grain size and the corresponding increase of the martensite laths [16,30,55,56].

Representative stress-strain curves obtained from tensile testing are shown in Fig. 8b and the average strength/strain-values are summarized in Table 3. The deformability in tension is slightly increased from $8.2 \pm 0.9\%$ (SLM) to $9.3 \pm 0.9\%$ (SLRM (2)) most likely due to the decreased porosity. On the other hand, the slightly reduced grain sizes of the SLRM (2) specimens can further promote deformability [29–31]. The obtained plasticity of the tested specimens is found to be higher than in [29,30,32,37,57]. Dimple-like features were observed in all specimens. Dimples are generally a sign of ductile fracture and their presence is in agreement with the larger plastic strain in tension as well as in compression if compared to conventionally processed samples [43]. Next to the deformability, the fracture strength of the remelted specimens (492 ± 55 MPa) is not drastically influenced and can be found near the SLM samples (617 ± 48 MPa) with a tendency of lower values. One reason for this can be the larger deviation of the relative density for the SLRM (2) specimens (see Section 3.2). For both tensile curves, the double yielding behaviour can be clearly seen and seems to follow our findings from compression testing. In order to fully understand the influence of the remelting step on the detwinning behaviour and the pseudoelasticity, a series of further tests have to be carried out. This, however, is beyond the scope of the present work and is subject to upcoming publications.

4. Conclusions

In this study, an additional remelting step was implemented in the processing of a 81.95Cu-11.85Al-3.2Ni-3Mn shape-memory alloy via

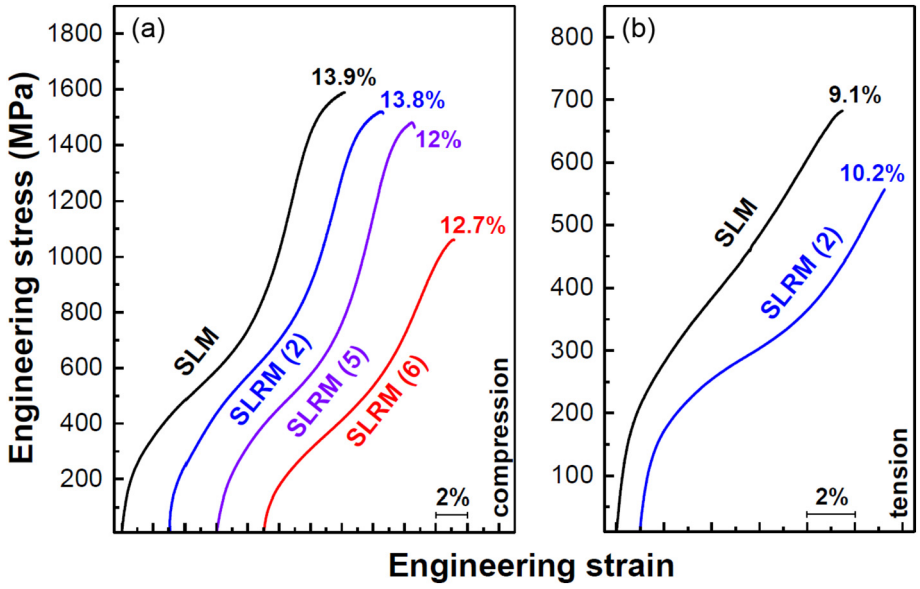

Fig. 8. Stress-strain curves for SLM and selected SLRM specimens in (a) compression and (b) tension. Fracture of the fully martensitic samples occurs at the indicated strains. The average values are listed in Table 3.

selective laser melting. The single-track method and subsequent remelting of bulk material was used to investigate and optimize the process parameters. In this way, selected parameters can be used to adjust the remelting depth and with it the corresponding materials properties.

In terms of relative density, no clear correlation between the energy input and the relative density could be observed. However, the optimum energy input in order to increase the relative density to 99.5 ± 0.3% is around 36 J/mm^3. This is in the range of the energy input of a SLM bulk samples with 98.9 ± 0.1% relative density. The detailed analysis of pore sizes by X-ray computed tomography reveals that the increase in the density is accompanied by an elimination of pores smaller than 100 μm.

The measured average grain size is only slightly affected by the additional remelting step when lower energy inputs are used, but it remarkably coarsens when the energy is adjusted between 100 and 250 J/mm^3. The transformation temperatures can be influenced likewise by the process parameters. In general, the peak-values of the martensitic transformation can be adjusted between 90 and 120 °C by remelting.

Samples produced by SLM and SLRM show a pronounced deformability in compression and tension. Although the pore and grain sizes of the remelted specimens vary from the values of the SLM reference sample, the mechanical properties are not drastically changed.

The investigations in this work prove that an additional remelting step for a 81.95Cu-11.85Al-3.2Ni-3Mn shape-memory alloy can be used to produce compact and fully martensitic samples with increased relative density and small grain sizes. By adjusting the energy layer input during remelting, the transformation temperatures of SLM bulk samples can be tuned without compromising the mechanical properties or the need of additional post-processing steps.

Acknowledgements

The authors are grateful to A. Voß, H. Bußkamp and K. Hennig for carrying out the chemical analysis, N. Geißler for technical assistance and A. Funk for assistance with X-ray computed tomography. Furthermore, we thank P. Gargarella, C. Bolfarini, C.S. Kiminami and J. Eckert for stimulating discussions. Financial support by DFG under grant no. PA 2275/4-1 is gratefully acknowledged.

References

[1] T. Gustmann, A. Neves, U. Kühn, P. Gargarella, C.S. Kiminami, C. Bolfarini, J. Eckert, S. Pauly, Influence of processing parameters on the fabrication of a Cu-Al-Ni-Mn shape-memory alloy by selective laser melting, Addit. Manuf. 11 (2016) 23–31.
[2] S. Pauly, L. Löber, R. Petters, M. Stoica, S. Scudino, U. Kühn, J. Eckert, Processing metallic glasses by selective laser melting, Mater. Today 16 (2013) 37–41.
[3] J.P. Kruth, L. Froyen, J. Van Vaerenbergh, P. Mercelis, M. Rombouts, B. Lauwers, Selective laser melting of iron-based powder, J. Mater. Process. Technol. 149 (2004) 616–622.
[4] M. Thomas, G.J. Baxter, I. Todd, Normalised model-based processing diagrams for additive layer manufacture of engineering alloys, Acta Mater. 108 (2016) 26–35.
[5] E. Yasa, J.P. Kruth, J. Deckers, Manufacturing by combining selective laser melting and selective laser erosion/laser re-melting, CIRP Ann. Manuf. Technol. 60 (2011) 263–266.
[6] I. Yadroitsev, I. Smurov, Selective laser melting technology: from the single laser melted track stability to 3D parts of complex shape, Phys. Procedia 5 ((2010) 551–560.
[7] J. Sander, J. Hufenbach, L. Giebeler, H. Wendrock, U. Kühn, J. Eckert, Microstructure and properties of FeCrMoVC tool steel produced by selective laser melting, Mater. Des. 89 (2016) 335–341.
[8] J. Sander, J. Hufenbach, M. Bleckmann, L. Giebeler, H. Wendrock, S. Oswald, T. Gemming, J. Eckert, U. Kühn, Selective laser melting of ultra-high-strength TRIP steel: processing, microstructure, and properties, J. Mater. Sci. 52 (2016) 4944–4956.
[9] R.D. Li, Y.S. Shi, J.H. Liu, H.S. Yao, W.X. Zhang, Effects of processing parameters on the temperature field of selective laser melting metal powder, Powder Metall. Met. Ceram. 48 (2009) 186–195.
[10] H. Schwab, F. Palm, U. Kühn, J. Eckert, Microstructure and mechanical properties of the near-beta titanium alloy Ti-5553 processed by selective laser melting, Mater. Des. 105 (2016) 75–80.
[11] T.H.C. Childs, C. Hauser, M. Badrossamay, Mapping and modelling single scan track formation in direct metal selective laser melting, CIRP Ann. Manuf. Technol. 53 (2004) 191–194.
[12] C. Haberland, M. Elahinia, J.M. Walker, H. Meier, J. Frenzel, On the development of high quality NiTi shape memory and pseudoelastic parts by additive manufacturing, Smart Mater. Struct. 23 (2014) 1–13.
[13] L. Masseling, Y.-C. Hargedorn, K. Wissenbach, Fabrication of micro structures with NiTi shape memory alloy via μSLM, in: B. Müller (Ed.), Fraunhofer Direct Digital Manufacturing Conference, Fraunhofer Verlag, Berlin 2016, pp. 428–433.
[14] C. Haberland, M. Elahinia, J. Walker, H. Meier, Visions, concepts and strategies for smart Nitinol actuators and complex Nitinol structures produced by additve manufacturing, Conference an Smart Materials, Adaptive Structures and Intelligent Systems (SMASIS), The American Society of Mechanical Engineers (ASME), Snowbird, 2013.
[15] T. Bormann, R. Schumacher, B. Muller, M. Mertmann, M. de Wild, Tailoring selective laser melting process parameters for NiTi implants, J. Mater. Eng. Perform. 21 (2012) 2519–2524.
[16] S. Dadbakhsh, M. Speirs, J.-P. Kruth, J. Schrooten, J. Luyten, J. Van Humbeeck, Effect of SLM parameters on transformation temperatures of shape memory nickel titanium parts, Adv. Eng. Mater. 16 (2014) 1140–1146.
[17] B. Zhang, J. Chen, C. Coddet, Microstructure and transformation behavior of in-situ shape memory alloys by selective laser melting Ti–Ni mixed powder, J. Mater. Sci. Technol. 29 (2013) 863–867.
[18] M.H. Elahinia, M. Hashemi, M. Tabesh, S.B. Bhaduri, Manufacturing and processing of NiTi implants: a review, Prog. Mater. Sci. 57 (2012) 911–946.
[19] T. Bormann, B. Müller, M. Schinhammer, A. Kessler, P. Thalmann, M. de Wild, Microstructure of selective laser melted nickel–titanium, Mater. Charact. 94 (2014) 189–202.
[20] S. Dadbakhsh, M. Speirs, J. Van Humbeeck, J.-P. Kruth, Laser additive manufacturing of bulk and porous shape-memory NiTi alloys: from processes to potential biomedical applications, MRS Bull. 41 (2016) 765–774.
[21] M. Elahinia, N. Shayesteh Moghaddam, A. Amerinatanzi, S. Saedi, G.P. Toker, H. Karaca, G.S. Bigelow, O. Benafan, Additive manufacturing of NiTiHf high temperature shape memory alloy, Scr. Mater. 145 (2018) 90–94.
[22] J. Ma, I. Karaman, R.D. Noebe, High temperature shape memory alloys, Int. Mater. Rev. 55 (2013) 257–315.
[23] D.C. Lagoudas, Shape Memory Alloys, Springer Science+Business Media, LLC, New York, 2008.
[24] J. Mohd Jani, M. Leary, A. Subic, M.A. Gibson, A review of shape memory alloy research, applications and opportunities, Mater. Des. 56 (2014) 1078–1113.
[25] M. Vollmer, P. Krooß, C. Segel, A. Weidner, A. Paulsen, J. Frenzel, M. Schaper, G. Eggeler, H.J. Maier, T. Niendorf, Damage evolution in pseudoelastic polycrystalline Co–Ni–Ga high-temperature shape memory alloys, J. Alloys Compd. 633 (2015) 288–295.
[26] M.H. Wu, Cu-based shape memory alloys, in: T.W. Duerig, K.N. Melton, D. Stöckel, C.M. Wayman (Eds.), Engineering Aspects of Shape Memory Alloys, Butterworth-Heinemann Ltd, London 1990, pp. 69–88.
[27] R.D. Cava, C. Bolfarini, C.S. Kiminami, E.M. Mazzer, W.J. Botta Filho, P. Gargarella, J. Eckert, Spray forming of Cu–11.85Al–3.2Ni–3Mn (wt%) shape memory alloy, J. Alloys Compd. 615 (2014) 602–606.
[28] K. Sugimoto, K. Kamei, M. Nakaniwa, Cu-Al-Ni-Mn: a new shape memory alloy for high temperature applications, in: T.W. Duerig, K.N. Melton, D. Stöckel, C.M. Wayman (Eds.), Engineering Aspects of Shape Memory Alloys, Butterworth-Heinemann Ltd, London 1990, pp. 89–95.
[29] K. Mukunthan, L.C. Brown, Preparation and properties of fine grain beta-CuAlNi strain-memory alloys, Metall. Trans. A. 19A (1988) 2921–2929.
[30] G.N. Sure, L.C. Brown, The mechanical properties of grain refinded beta-CuAlNi strain-memory alloys, Metall. Trans. A. 15A (1984) 1613–1621.
[31] U. Sari, Influences of 2.5wt% Mn addition on the microstructure and mechanical properties of Cu-Al-Ni shape memory alloys, Int. J. Miner. Metall. Mater. 17 (2010) 192–198.
[32] G. Lojen, M. Gojić, I. Anžel, Continuously cast Cu–Al–Ni shape memory alloy – properties in as-cast condition, J. Alloys Compd. 580 (2013) 497–505.
[33] J. Dutkiewicz, T. Czeppe, J. Morgiel, Effect of titanium on structure and martensic transformation in rapidly solidified Cu-Al-Ni-Mn-Ti alloys, Mater. Sci. Eng. A 273 (1999) 703–707.
[34] E.M. Mazzer, C.S. Kiminami, P. Gargarella, R.D. Cava, L.A. Basilio, C. Bolfarini, W.J. Botta Filho, J. Eckert, T. Gustmann, S. Pauly, Atomization and selective laser melting of a Cu-Al-Ni-Mn shape memory alloy, Mater. Sci. Forum 802 (2014) 343–348.
[35] P. Gargarella, C.S. Kiminami, E.M. Mazzer, R.D. Cava, L.A. Basilio, C. Bolfarini, W.J. Botta, J. Eckert, T. Gustmann, S. Pauly, Phase formation, thermal stability and mechanical properties of a Cu-Al-Ni-Mn shape memory alloy prepared by selective laser melting, Mater. Res. 18 (2015).
[36] T. Gustmann, A. Neves, U. Kühn, P. Gargarella, C. Kiminami, C. Bolfarini, J. Eckert, S. Pauly, Fabrication of Cu-Al-Ni-Mn shape-memory parts by selective laser melting, in: B. Müller (Ed.), Fraunhofer Direct Digital Manufacturing Conference, Fraunhofer Verlag, Berlin 2016, pp. 159–164.
[37] M.R. da Silva, P. Gargarella, T. Gustmann, W.J. Botta Filho, C.S. Kiminami, J. Eckert, S. Pauly, C. Bolfarini, Laser surface remelting of a Cu-Al-Ni-Mn shape memory alloy, Mater. Sci. Eng. A 661 (2016) 61–67.
[38] J. Vaithilingam, R.D. Goodridge, R.J.M. Hague, S.D.R. Christie, S. Edmondson, The effect of laser remelting on the surface chemistry of Ti6Al4V components fabricated by selective laser melting, J. Mater. Process. Technol. 232 (2016) 1–8.
[39] E. Yasa, J. Deckers, J.P. Kruth, The investigation of the influence of laser re-melting on density, surface quality and microstructure of selective laser melting parts, Rapid Prototyp. J. 17 (2011) 312–327.

[40] K. Kempen, L. Thijs, B. Vrancken, S. Buls, J. Van Humbeeck, J.P. Kruth, Producing Crack-free High Density M2HSS Parts by Selective Laser Melting: Pre-Heating the Baseplate, Solid Freeform Fabrication Symposium Austin, Texas, 2013 131–139.
[41] W.H. Wu, Y.Q. Yang, Y.L. Huang, Direct manufacturing of Cu-based alloy parts by selective laser melting, Chin. Opt. Lett. 5 (2007) 37–40.
[42] Y. Sutou, T. Omori, R. Kainuma, K. Ishida, Ductile Cu–Al–Mn based shape memory alloys: general properties and applications, Mater. Sci. Technol. 24 (2008) 896–901.
[43] T. Gustmann, J.M. Dos Santos, P. Gargarella, U. Kühn, J. Van Humbeeck, S. Pauly, Properties of Cu-based shape-memory alloys prepared by selective laser melting, SM Superelas 3 (2017) 24–36.
[44] D.N. Adnyana, The Effect of Grain Size on the Martensite-start-temperature in a Grain Refined Copper-based Shape Memory Alloy, International Conference on Martensitic Transformations, The Japan Institute of Metals, 1986 774–779.
[45] H.V. Atkinson, S. Davies, Fundamental aspects of hot isostatic pressing: an overview, Metall. Mater. Trans. A 31A (2000) 2981–3000.
[46] K. Otsuka, M. Tokonami, K. Shimizu, Structure analysis of stress-inducted β″1 martensite in a Cu-Al-Ni alloy by neutron diffraction, Acta Metall. 27 (1979) 965–972.
[47] E.M. Mazzer, C.S. Kiminami, C. Bolfarini, R.D. Cava, W.J. Botta, P. Gargarella, F. Audebert, M. Galano, Phase transformation and shape memory effect of a Cu-Al-Ni-Mn-Nb high temperature shape memory alloy, Mater. Sci. Eng. A 663 (2016) 64–68.
[48] H. Schwab, M. Bönisch, L. Giebeler, T. Gustmann, J. Eckert, U. Kühn, Processing of Ti-5553 with improved mechanical properties via an in-situ heat treatment combining selective laser melting and substrate plate heating, Mater. Des. 130 (2017) 83–89.
[49] P. La Roca, L. Isola, P. Vermaut, J. Malarría, Relationship between martensitic plate size and austenitic grain size in martensitic transformations, Appl. Phys. Lett. 106 (2015), 221903.
[50] T. Tadaki, Cu-based shape memory alloys, in: K. Otsuka, C.M. Wayman (Eds.), Shape Memory Materials, Cambridge University Press, Cambridge 1998, pp. 97–116.
[51] K. Otsuka, X. Ren, Mechanism of martensite aging effect, Scr. Mater. 50 (2004) 207–212.
[52] P. Fischer, D. Dunne, N. Kennon, The Effects of Transformation Cycling and Ageing on the β1-γ1′ Thermoelastic Martensitic Transformation in Cu-Al-Ni, International Conference on Martensitic Transformations, The Japan Institute of Metals, Nara, 1986 946–951.
[53] G.F. Vander Voort, Metallography: Principles and Practice, ASM International, 1999.
[54] S.N. Saud, T.A. Abu Bakar, E. Hamzah, M.K. Ibrahim, A. Bahador, Effect of quarterly element addition of cobalt on phase transformation characteristics of Cu-Al-Ni shape memory alloys, Metall. Mater. Trans. A 46A (2015) 3528–3542.
[55] Y. Sutou, T. Omori, J.J. Wang, R. Kainuma, K. Ishida, Characteristics of Cu–Al–Mn-based shape memory alloys and their applications, Mater. Sci. Eng. A 378 (2004) 278–282.
[56] J.-L. Liu, H.-Y. Huang, J.-X. Xie, The roles of grain orientation and grain boundary characteristics in the enhanced superelasticity of Cu71.8Al17.8Mn10.4 shape memory alloys, Mater. Des. 64 (2014) 427–433.
[57] S.K. Vajpai, R.K. Dube, S. Sangal, Application of rapid solidification powder metallurgy processing to prepare Cu–Al–Ni high temperature shape memory alloy strips with high strength and high ductility, Mater. Sci. Eng. A 570 (2013) 32–42.